Parameter-free optic disc detection

Cattleya Duanggate [a,*], Bunyarit Uyyanonvara [a], Stanislav S. Makhanov [a], Sarah Barman [b], Tom Williamson [c]

[a] School of Information, Computer and Communication Technology, Sirindhorn International Institute of Technology (SIIT), Thammasat University, 131 Moo 5, Tiwanont Road, Bangkadi, Muang, Pathumthani 12000, Thailand
[b] Faculty of Computing, Information Systems and Mathematics, Kingston University, Penrhyn Road, Kingston upon Thames, Surrey, KT1 2EE, UK
[c] Department of Ophthalmology, St. Thomas' Hospital London SE1 7EH, UK

ARTICLE INFO

ABSTRACT

The paper presents a simple, parameter-free method to detect the optic disc in retinal images. It works efficiently for blurred and noisy images with a varying ratio OD/image size. The method works equally well on images with different characteristics which often cause standard methods to fail or require a new round of training. The proposed method has been tested on 214 infant and adult retinal images and has been compared against hand-drawn ground truths generated by experts. It displays consistently high OD detection rates without any prior training or adjustment of the parameters.

© 2010 Elsevier Ltd. All rights reserved.

1. Introduction

Precise localization of an optic disc (OD) boundary is an important problem in ophthalmic image processing. Once the OD has been identified, other regions of clinical importance such as the fovea or macula can be easily determined. The OD is important for establishing a frame of reference within the retinal image, for instance for diagnosis of abnormalities such as hypertensive retinopathy [1]. Because of its immense importance, a variety of image processing techniques have been proposed.

The OD detection techniques can be classified into several groups as follows: blood vessel tracing [2,3], template matching [4,5], boundary tracing [6–8], active contour or snake [9–12], machine learning [13–18], multilevel thresholding [19] and shape detection [20–22].

The OD detection algorithm, presented by Foracchia et al. [2], is based on a model of vascular structure. The authors used a geometrical parametric model to locate the centre point of the OD. Akita and Kuga [3] trace the parent–child relationship between blood vessels segments, tracking back to the centre of the OD. The method requires a robust detection of the blood vessels, which is difficult

in images of the diseased retina where even quite sophisticated algorithms detect false positives along the edges of white lesions and along the OD. Lalonde et al. [4] use a pyramidal decomposition and Hausdorff-based template matching guided by scale tracking of large objects using a multi-resolution image decomposition. This method is effective, but rather complex and hard to implement. In three dimensional reconstructions of conventional stereo OD image procedures, the resulting three-dimensional contour images that show OD structure clearly and intuitively is presented in [6], helping physicians to understand the stereo disc photograph. A semi-automated method is used by Cox and Wood [7] to indicate external points on the boundary which are automatically connected by a tracing procedure. Morris et al. [8] present a completely automatic method which traces between points on the boundary identified automatically by their gradient. Sinthanayothin et al. [13] use the intensity variation between the dark vessels and the bright nerve fibers to locate the OD, the work also locates the fovea, and retinal blood vessels. However, this algorithm often fails when detecting the OD in fundus images with a large number of white lesions. Active contour models (snakes) have been applied to images centred on the optic nerve head [9–12]. They are reported to be successful for high resolution and high contrast images. The main drawback of these algorithms is the convergence to false boundaries caused by the noise and missing edges which often occur in infant images captured to screen for Retinopathy of Prematurity (ROP) [23].

Principal component analysis (PCA) and active shape techniques are often combined to detect the OD centre and to approxi-

* Corresponding author. Tel.: +66 2501 3505x2005; fax: +66 2501 3505.
E-mail addresses: D5022300403@studentmail.siit.tu.ac.th,
cat.cattleya@gmail.com (C. Duanggate), bunyarit@siit.tu.ac.th (B. Uyyanonvara),
makhanov@siit.tu.ac.th (S.S. Makhanov), s.barman@kingston.ac.uk (S. Barman),
tom@retinasurgery.co.uk (T. Williamson).

mate the OD area by using a "disc space" [14,15]. Kavitha and Shenbaga [19] use morphological operations and multilevel thresholding to extract the brighter regions that include the OD and exudates. Jelinek et al. [5] use Canny edge detection, template matching and the Haar transform to detect the OD boundary. Corona et al. [16] use an algorithm, combining power cepstrum and zero-mean-normalized cross correlation techniques, which extract depth information using coarse-to-fine disparity between corresponding windows in a stereo pair. The grey level encoded sparse disparity matrix is subjected to a cubic B-spline operation to generate smooth representations of the OD surface and new three-dimensional matrices from isodisparity contours. A combination of the methods is given that determines whether a macula centred retinal image is from the left or right eye and automatically detects the OD, the fovea and the vascular arch by inferring the location of a set of landmarks placed on these structures [17]. The result of the automatic detection of the optic nerve using digital red-free fundus photography is presented in [18]. The location of the OD is predicted by using a two-class, Bayesian classifier. The main drawback of this approach is its computational complexity. Chrástek et al. [24] present an image registration technique for automated segmentation of the OD in two imaging modalities, namely, in images of scanning laser tomography and in colour images. However, this method requires user interaction to locate several couples of corresponding features (landmarks). Manual location of landmarks may result in low precision of the final registration. Mathematical morphology techniques have been used widely for extracting image components because it is fast and requires low computing power. Sopharak et al. [20] use morphological operators to find the OD area. Another popular method that used to localize the OD is the Circular Hough Transform (CHT) [21,22]. Sekhar et al. [21] detect the OD by finding the brightest region within the image. The magnitude of the OD is calculated using morphological operations. The Circular Hough Transform is then applied to the gradient image in to detect the contour and the centre of the OD. However, Xiaolu and Rangaraj [22] show that CHT performance is very poor when the shape is only slightly non-circular. Niemeijer et al. [25] present an automatic system to detect location of the OD and fovea in colour retinal images. This approach uses a k-Nearest Neighbour regressor and a circular template to estimate the distance in pixels to the object of interest at any given location in the image based on a set of features measured at that location. It finds the OD in the first step and then searches for the fovea based on the OD location. The algorithm is trained on a set of adult retinal images with and without lesions.

Finally, a recent literature survey of Winder et al. [26] cites 38 papers on localization of the optic disc and identification of its boundary. The localization is most frequently achieved by identifying the point of convergence of the main retinal blood vessels, or by using active contour models, snakes, principal components analysis (PCA) or the watershed transforms. A number of articles combined PCA and snakes to achieve localization of the disk and definition of the boundary. However, segmentation of the vessel structure could be computationally hard requiring a very well validated algorithm. This is why methods such as simple identification of regions of high intensity pixels and adaptive thresholding are still popular.

Furthermore, most of the above techniques have been applied to adult retinal images where the retina is well developed and the image has a very high contrast. Although image acquisition of the infant retinal images is fast, it is often done in poor lighting conditions. Besides, the infant retina is not very well developed. This results in low-contrast, blurred and dark images. Therefore, many standard detection algorithms fail to correctly detect the OD for infant retinal images. Furthermore, all of the above mentioned schemes require a set of control parameters such as the operator window size, the size of templates, certain thresholds, etc. These parameters must be optimized using a set of training images. Consequently, the algorithms are efficient and robust as applied to a set of images with similar characteristics (contrast, light conditions, etc.) but fail completely on different sets. The number of the control parameters is usually greater than 3 and the range of the parameters is usually large (see Table 1).

This paper employs a concept of feature based detection combined with a scale-space approach. The mathematical foundations of the scale-space analysis were first proposed by Witkin and Koenderink [29,30] to obtain a multi-scale representation of a measured signal by embedding it into a scale-parameter family of blurred signals. Later, Lindeberg [31,32] used this concept to analyze structures in digital images. The scale-space analysis employs blurring the input image so that the objects are smoothed and eventually turn into the so-called light blobs.

The algorithm appears to be fast and parameter free. It works efficiently for blurred and noisy images with a varying OD/image size ratio. The method works equally well on images with different characteristics which often cause standard methods to fail or

Table 1
Selected standard OD detection algorithms.

| Algorithms	Parameters count	Parameters	Used to detect OD?	Note
Geometrical parametric model	>3	Number of data points, initial model parameters value, termination criterion, etc.	Yes [2]	Mark the centre of OD only
Bayesian classifier	>4	Prior probability for the location of OD, intensity threshold, vascular orientation, size of morphological operators, etc.	Yes [17]	
Morphological operations	>3	Intensity threshold, size of structure elements, etc.	Yes [20]	
Circular Hough Transform	>3	Canny thresholds, window size, object radius, etc.	Yes [21,22,24]	
Active contour or snake	>4	Number of nodes, internal and external force, termination criteria, etc.	Yes [9–12]	
Principal component analysis (PCA)	>3	Size of the cropped image, size of the optic disc, edge detection threshold, etc.	Yes [14,15,23]	
Pyramidal decomposition and Hausdorff-based template matching	>2	Canny thresholds, etc.	Yes [4]	
Neural networks	>2	Number of the training patterns, size of the training pattern, etc.	No [27]	
Fuzzy cellular neural networks	>6	Size of structure elements, fuzzy feedback MIN and MAX template, fuzzy feed-forward MIN and MAX template, etc.	No [28]	
k-Nearest Neighbour regressor	>3	Number of neighbours, parameter vector, error in a prediction, etc.	Yes [25]	
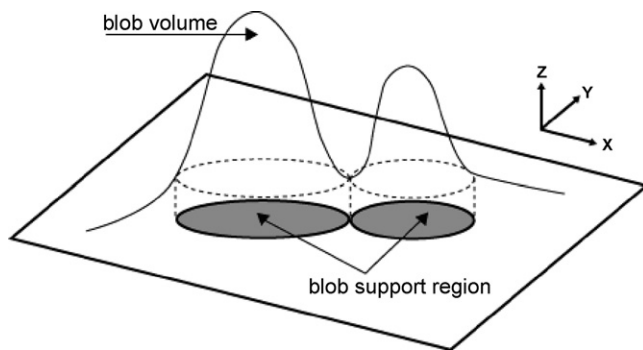
Fig. 1. Grey-level blobs produced by Gaussian blurring.

require a new round of training. The proposed method has been tested by 214 infant and adult retinal images and has been compared against hand-drawn ground truths generated by experts. It displays consistently high OD detection rates without any prior training or adjustment of the parameters.

2. Methods

This section is structured as follows: Sections 2.1–2.3 give a general scale-space representation and blob detection mechanism; Section 2.4 introduces the feature descriptors used in the post processing step and Section 2.5 presents the classification techniques.

2.1. Multi-scale representation

In order to detect an optic disc in a parameter-free environment, we disregard all camera-dependent parameters such as size of the OD and the OD's colour. We assume, however, that the OD produces a dominant light blob which appears in many scales. In other words it has a long life over the scale space. The classic scale-space theory [31] defines a multi-scale representation $f(x,y,\sigma)$ of a two-dimensional image $f(x,y)$ by a convolution with the Gaussian kernel characterized by a variance σ. The successive smoothing process generates a set of output images at various scales related to σ. At the finest scale the output is the original image itself. The increment of the scale parameter results in suppressing the image structures and creating so called light blobs. Throughout the process, the Gaussian blurring simplifies the image without producing new spurious structures. Smaller light blobs that are close together merge into larger ones (Fig. 1) until the entire image eventually contains only one blob.

2.2. Blob extraction

At each scale, blobs are segmented. The blob seeds are initialized at every local maximum. Next the region around the seed grows

until it meets a local minimum. The blob extraction consists of the following steps:

1) Connected pixels with an equal intensity are grouped into regions.
2) The regions are sorted with respect to their grey-levels in descending order.
3) For each region, a list of its neighbouring regions is created.
4) The regions are classified to be background, part of the blob or merged into blobs with the following criteria
    4.1) If the region has no neighbours, then it is a local maximum point and will be a seed of the blob.
    4.2) If the region has a neighbour region with higher grey-level but that region has been classified as background, then the current region should be assigned to be background.
    4.3) If the region has more than one neighbour region with a higher grey-level, and those neighbour regions are not parts of the same blob, then the current region must be set to the background.
    4.4) If the neighbour regions have a higher grey-level than the current regions and are parts of the same blob, then the current region is combined with the blob.

Note that the blob extraction algorithm is similar to the standard watershed method where the blob merging step is equivalent to the expansion of the watershed. In fact the standard watershed method can be applied in the framework of the scale-space algorithm as well. However, the watershed techniques applied to the original image may produce many small blobs which are hard to interpret (see examples in Fig. 2). As opposed to this the space-scale technique makes it possible to track only the most significant blobs with the largest lifetime (Fig. 3).

The entire collection of blobs from all scales (see Figs. 4 and 5) is passed to blob linking and feature extraction steps presented in the next sections.

2.3. Scale-space blob linking and blob life time

To construct the scale space, first, we initialize the scales σ_{max} and σ_{min}. The maximum scale σ_{max} corresponds to the coarsest scale where it results in only one blob. The finest scale $\sigma_{min} = 0$. The intermediate scales are constructed as follows

1) Starting from interval $[\sigma_{min}, \sigma_{max}]$ we binary-search for the next σ which allows not more than two blobs. Once this scale is found, we blur the original image with this σ in the Gaussian kernel. The sequential blob detection algorithm, described in the previous section, is used to extract the blobs. This scale is then set as a new σ_{min}.
2) Repeat step 1) until $\sigma_{max} - \sigma_{min} < \varepsilon$ where ε is a small value close to zero.
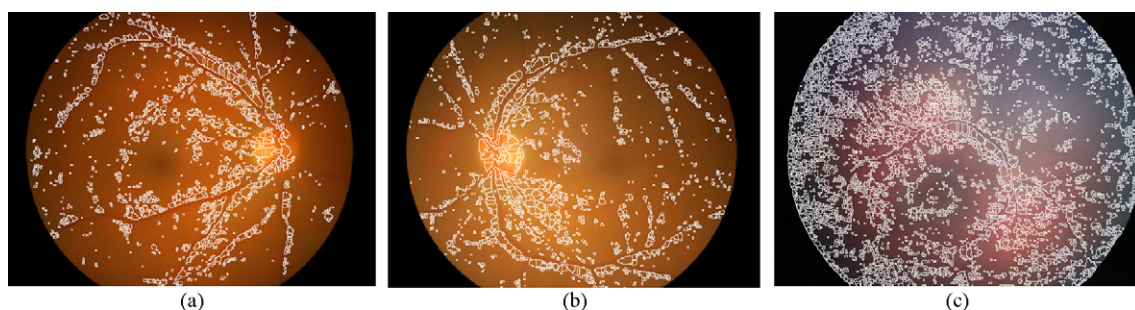

Fig. 2. Three examples of the watershed blob detection applied to raw images.
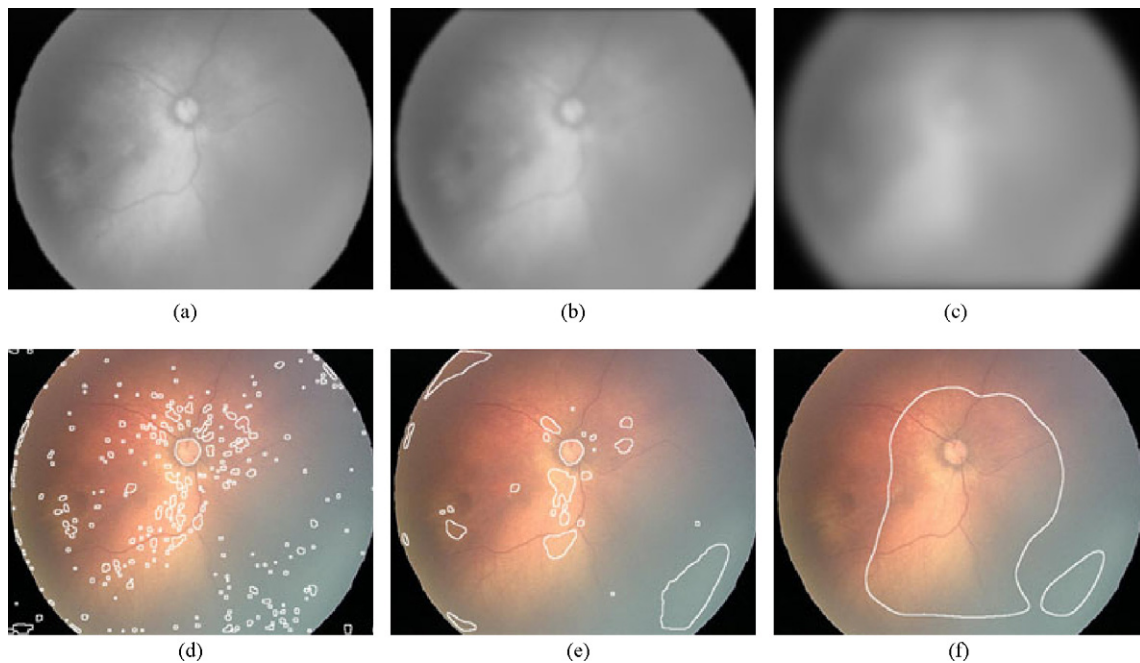
Fig. 3. Detected blobs in different scales. (a), (b) and (c) Gaussian blurred images with σ = 2.21, 4.09 and 14.99 respectively. (d), (e) and (f) The results of blob detection for (a), (b) and (c) respectively.

3) Link blobs in a finer scale with their counterparts in the adjacent, coarser scale [32]. The blob linking through the scale levels is based on a spatial coincidence. If two blobs at adjacent scales have a common pixel, they are registered as the blobs which belong to the same sub tree. Blobs belonging to consecutive scales are linked to form a scale-space blob tree (see Fig. 6).

Given the scale-space tree, a blob's lifetime is evaluated to indicate the significance of each blob. The lifetime of the blob is evaluated as the number of steps that the blob survives over the scales before disappearing or merging with other blobs. The significant blobs surviving longer than others in each sub tree are chosen as the final candidates. For instance, blobs b_1 and b_2 in Fig. 6 have the same significance while b_4 is more significant than b_1 and b_2.

2.4. Blob descriptor

An appropriate classifier for the optic disc is still a subject of continuing research. There exist numerous models combining features of the OD and the geometric features of the blood vessels which enter the retina through the OD. For instance, Hoover and Goldbaum [33] exploit the convergence of the vessels to the OD. Similar approaches are introduced in [2,34]. Niemeijer et al. [25] consider 9 vessel based features and 2 optic disc based features (the average intensity and its standard deviation). However, segmentation of the vascular structure is itself a hard, computationally costly problem requiring a very well constructed algorithm. On the other hand, for fast OD detection it is often important to select the simplest set of features which is related only to the OD. Besides, under the space-
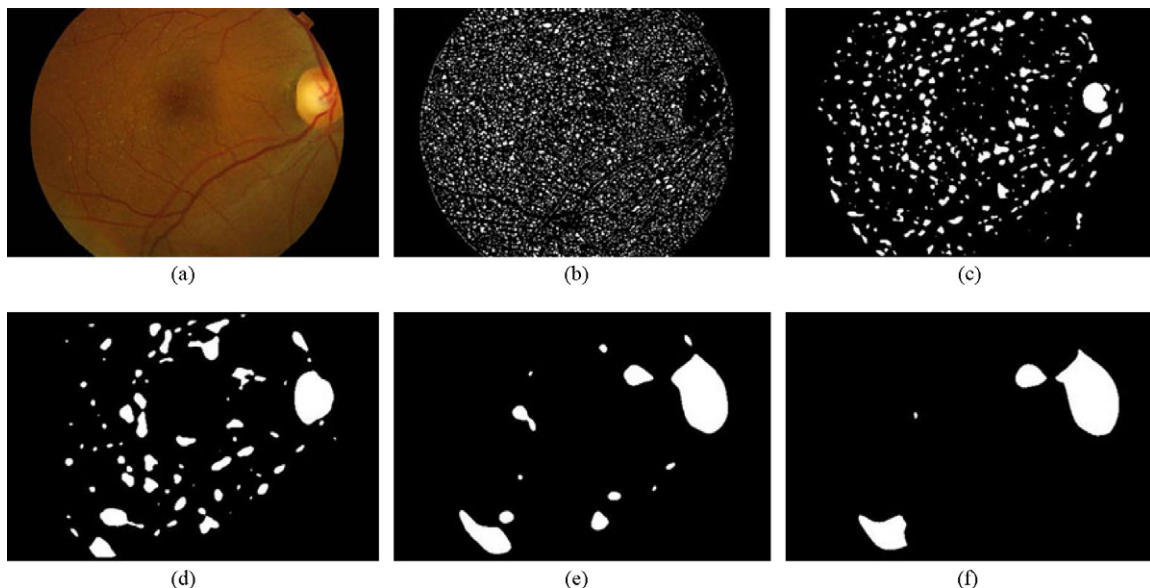

Fig. 4. Blob extraction in several scales (a) original image. (b)–(f) Blob detection results at scale σ = 0, 2, 4, 8 and 16, respectively.
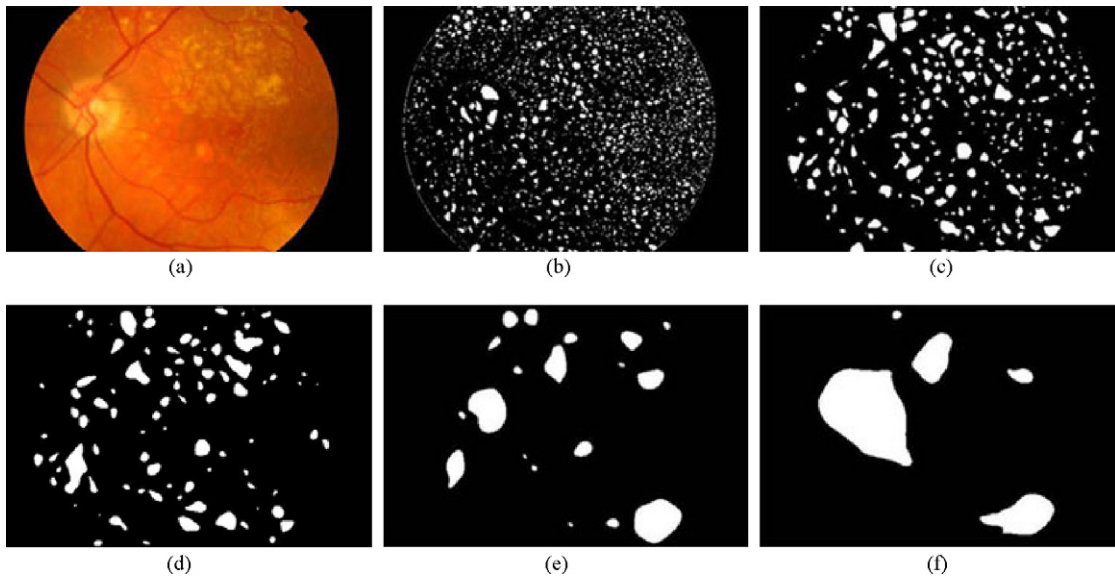
Fig. 5. Blob extraction (a) original image. (b)–(f) Blob detection at $\sigma = 0$, 2, 4, 8 and 16, respectively.

scale blurring the vessels inevitably disappear which makes it hard to incorporate the vessel based features.

The OD is defined as an oval-shaped area with the highest intensity containing branches of blood vessels at its centre [35]. Therefore, compactness and high intensity are the most common properties of the OD employed by many researchers. The compactness is given by

$$c = \frac{p^2}{4\pi A} \tag{1}$$

where P and A are the perimeter and the area of the blob, respectively.

Furthermore, Chaudhuri et al. [36] assumed that the grey level in the OD region is higher than in other parts of the retinal image. Sánchez et al. [37] and Welfer et al. [38] detect the OD by relying on the assumption that the OD is the brightest region. Perez-Rovira and Trucco [39] write "The OD normally appears as a bright circular zone with a radius close to 60 pixels and approximately centred vertically in the image. So a computationally cheap and efficient way to find plausible OD candidates is to smooth the image (removing noise and small bright spots) and detect the peaks in the intensity level map". It was observed that a healthy and well-imaged OD has a mean intensity level close to 0.15 higher than the mean of the entire image. A survey [26] notes that that the brightness and the

roundness of the OD is combined with a high variation of the grey level. This was employed by Sinthanayothin et al. [13] and later by Lowell et al. [40]. Actually, considering the intensity variation as a feature is a simple way to take into account the strong presence of the vascular structure converging to the centre of the OD [13]. The entropy is just another way to represent this feature. Sopharak et al. [20] showed that the entropy can be used to differentiate the OD from the background.

The entropy is given by

$$e = -\sum_{i=0}^{L-1} p(z_i)\log_2 p(z_i) \tag{2}$$

where z_i denotes the grey level and $p(z_i)$, $i = 0, 1, 2, \ldots, 255$ is the corresponding histogram.

In summary, the simplest and the most prominent features of the OD are the brightness, the roundness and the presence of the vascular structures on the light background. The third feature can be detected by the high total variation of the grey level or the high entropy. Of course, our choice of the features is intuitive since we
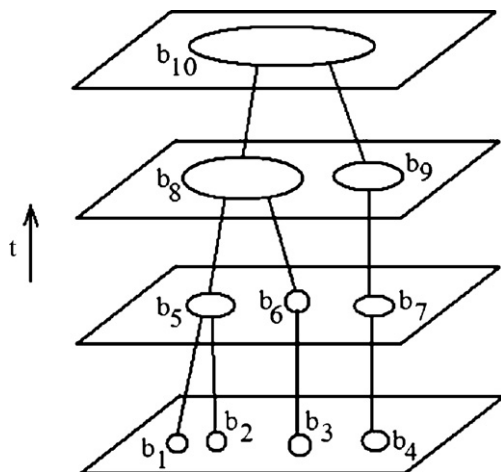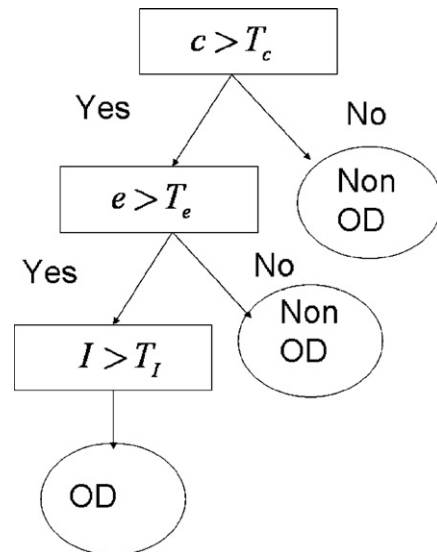

Fig. 6. A scale-space tree.

Fig. 7. The decision tree, T_c, T_e and T_I are the corresponding thresholds for compactness, entropy and intensity, respectively.

Table 2
Sensitivity to the thresholds for different classifiers.

Classifier/recognition rate	Decision tree T_c, T_e, $T_I \pm 5\%$	Regression $T_R \pm 5\%$	Majority voting T_c, T_e, $T_I \pm 5\%$
Min	97.67	100.00	97.67
Max	100.00	100.00	100.00

did not perform a systematic feature selection. However, the proposed set is simple, easy to calculate and is strongly supported by previous works. Besides, these features do not depend on the scale, colour and location of the OD on the image. This complies well with the blob detection method in the scale-space. All the dominant light blobs of all scales become the OD candidates irrespective of the colour, size or location of the OD.

2.5. Classifiers

After all three features are normalized to a 0–1 range, we use three classification methods to test for the OD, namely, the decision tree, regression and majority voting.

The decision tree constructed by the standard C4.5 [41] employing Shannon's entropy is shown in Fig. 7. The threshold for compactness, entropy and intensity were optimized using a grid search for the best performance using a training data set. If more than one blob gets through the decision tree, the one with highest intensity will be chosen.

The regression based classification follows Niemeijer et al. [25]. We used the simplest linear regression and a classifier employing the confidence level, T_R. Finally, the majority voting uses the same thresholds as those obtained for the decision tree. From a training set of 80 ODs and randomly selected 80 non-OD blobs, the best thresholds are $T_c = 0.6$, $T_e = 0.6$, $T_I = 0.6$, $T_R = 0.8$.
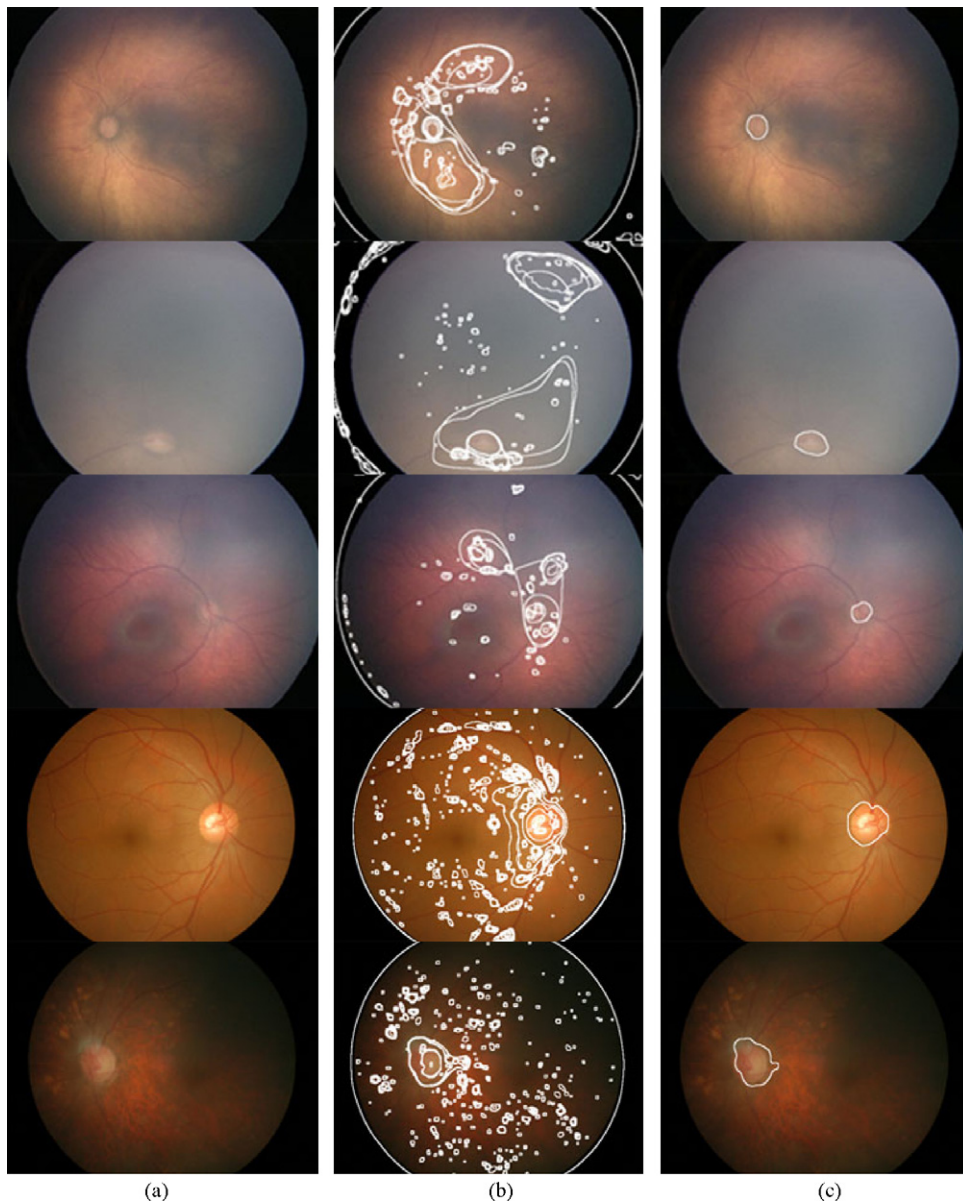

Fig. 8. Optic disc detection of 5 sample images (a) original images (b) all the detected blobs from all scales overlaid on original image (c) images showing the most significant blob (images in rows 1–3 are ROP images, images in rows 4–6 are adult retinal images).
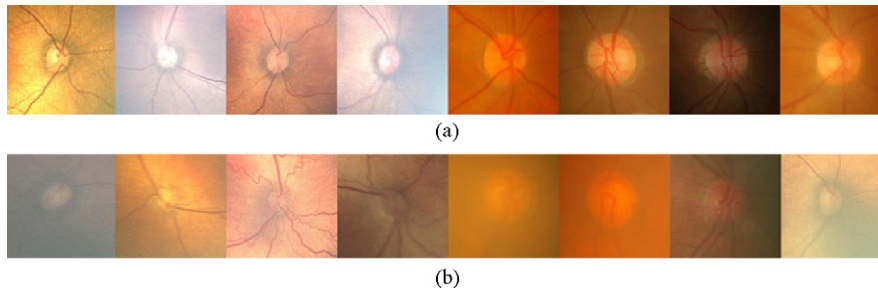
(a)

(b)

Fig. 9. Example of images (a) from group A1 where OD boundaries are visibly clear and (b) group A2 with faint OD boundary.

The sensitivity of the classifiers to the thresholds is presented in Table 2. The thresholds have been varied by 5% which constitutes a total of a 10% change. However, even with this relatively large change, the accuracy does not change significantly and is still appropriate. Moreover, the simple majority voting has approximately the same accuracy with reference to the decision tree and the regression.

3. Results

We demonstrate the robustness of the algorithm by testing on two different datasets, namely set A with 123 adult retinal images (size 752×500 pixels at 24-bit) and set B of 91 Retinopathy of Prematurity (ROP) images (size 640×480 pixels at 24-bit). Experiment 1 compares the proposed algorithm with baseline algorithms on the two sets to show that the algorithm works well without training. Experiment 2 tests the algorithms on resized and also randomly cropped images. Experiment 3 analyses the detection rates on an increasingly noisy set of images and finally, experiment 4 sees how the algorithm performs with outliers (Fig. 8).

3.1. Experiment 1: two different datasets

Data set A is divided into 2 groups. Group A1 consists of 105 images with a visible OD edge. The remaining 18 images with an unclear OD boundary are in group A2. We measure the accuracy of the OD detection at pixel level by comparing them to an ophthalmologist's hand drawn ground truth in terms of sensitivity and the positive predictive value (PPV). Note that general Specificity is not used because the portion of OD pixels is very small compared to the rest of the image. Specificity is then always close to 100% because False Positive (FP) and False Negative (FN) are relatively high compared to True Positive (TP) and True Negative (TN).

As a baseline comparison, we use a morphological operator and the Circular Hough Transform. These two methods are reported to be the most suitable for the OD detection [20,21,42]. The morphological operator uses an 8×8 structural element and three intensity thresholds, i.e., 0.75, 0.80 and 0.85. The Circular Hough Transform employs three Canny thresholds, 0.15, 0.25 and 0.35 to ensure the best performance of the algorithm. The radius of the target object is set to 20–45 pixels.

Examples of close-up images around the OD from the both groups are shown in Fig. 9. The detection rates of our proposed algorithm compared to the baseline algorithms are displayed in Table 3.

The ODs in group B appear faint with an unclear boundary. In turn, group B is divided into group B1 (60 images with a poor quality) and B2 (31 images with a very poor quality). The control parameters for the morphological operator method and the Circular Hough Transform have been obtained from training set A. Quantitative results from group B1 and B2 are shown in Table 4. Additional examples of the OD detection are shown in Fig. 10.

Although, the parameters used in morphological operations and the Circular Hough Transform are well-adjusted to the adult retinal images, they are totally unsuitable when applied to set B. Therefore, the accuracy of the proposed algorithm is comparable with the accuracy of the standard OD detection methods when they are applied to the same group of images. However, our method outperforms the conventional methods when fed with images obtained under different conditions. Finally, the OD detection on a combination of images A (adults) and B (infants) is good proof of the robustness of the proposed approach.

3.2. Experiment 2: resized and randomly cropped images

Furthermore, we prove the robustness of our algorithm by testing on images with different sizes. For each set, we generate

Table 3
Detection results of 123 adult retinal images.

Method	Clear-OD-boundary (105 images)		Faint-OD-boundary (18 images)	
	Average sensitivity (%)	Average PPV (%)	Average sensitivity (%)	Average PPV (%)
The proposed method	71.19	70.90	52.69	56.46
Morphological operator	90.51	59.58	83.05	31.50
Circular Hough Transform	69.77	78.23	39.28	45.43

Table 4
Detection results for 60 good quality and 31 poor quality images.

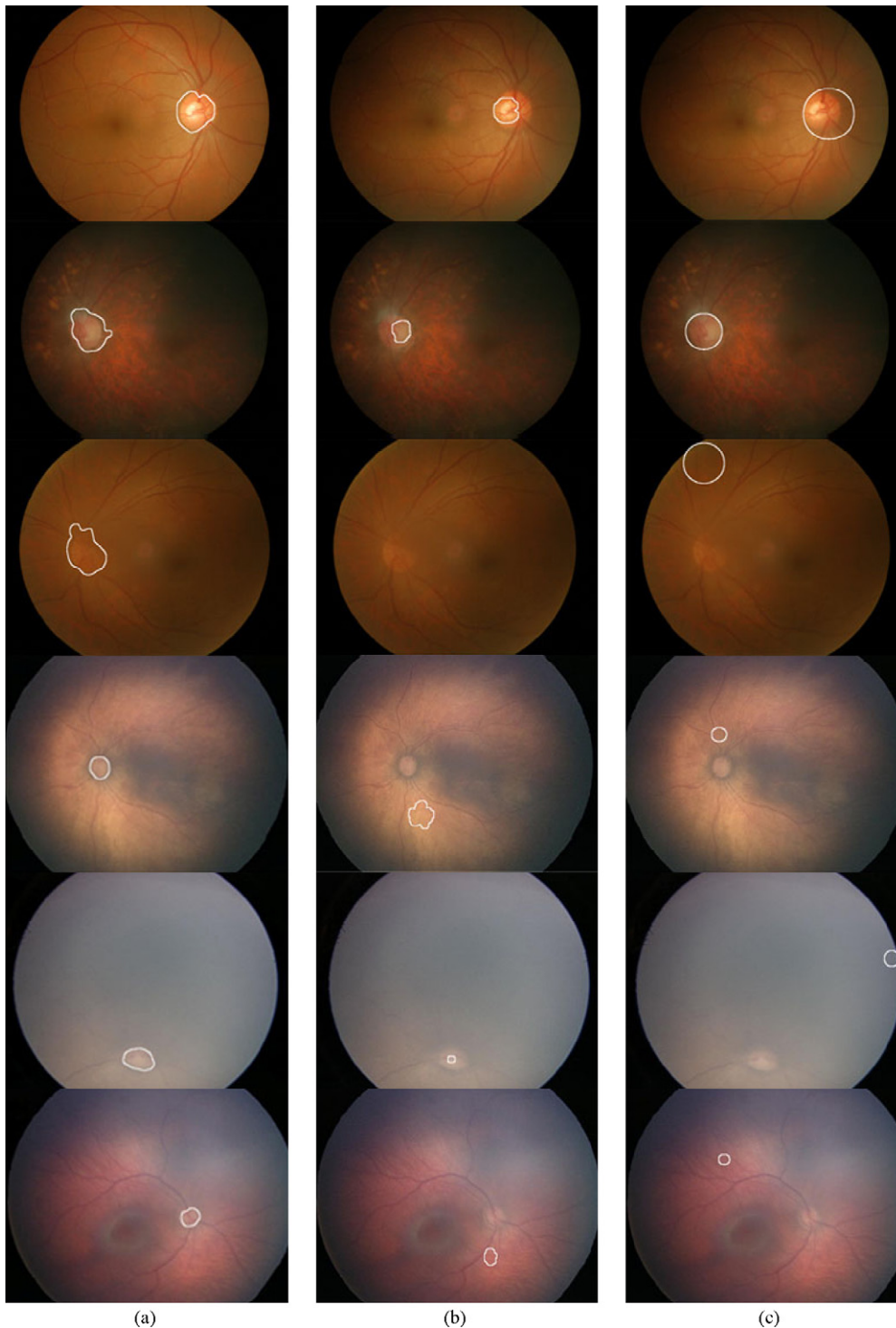| Method	Clear-OD-boundary (60 images)		Faint-OD-boundary (31 images)	
	Average sensitivity (%)	Average PPV (%)	Average sensitivity (%)	Average PPV (%)
The proposed method	72.57	92.38	56.49	38.68
Morphological operator	17.91	13.12	10.54	9.37
Circular Hough Transform	20.23	20.11	9.43	8.20

Fig. 10. The detection results. Column (a) our proposed method, (b) morphological operations, (c) Circular Hough Transform and Canny edge detection. Images in the row 1 are from A1. Images in rows 2 and 3 are from A2. Row 4 is from B1 and Rows 5 and 6 are from B2.

three additional data sets with the size 40%, 60% and 80% of the original images and compare the proposed method with the two conventional detection methods characterized by the same setup. Figs. 11 and 12 illustrate the advantage of the proposed method as applied to the resized images. For presentation purposes the images have been rescaled to the same dimensions.

Next we also apply our proposed algorithm to a set of randomly cropped images from A and B. Since cropping changes the ratio OD size/image size, the standard methods perform extremely poorly: 37.2% average sensitivity and 40.6% average PPV whereas

our method displays a solid performance of 85.37 and 82.87 respectively (see Table 5). Some detection examples are shown in Fig. 13.

3.3. Experiment 3: sensitivity to random noise

Tables 6–9 compare the accuracy of the method when the images are distorted by a 1%, 5% and 10% salt-and-pepper noise (see also Fig. 14). Note that since the proposed algorithm has intrinsic filtering steps built in because it increasingly blurs the image dur-
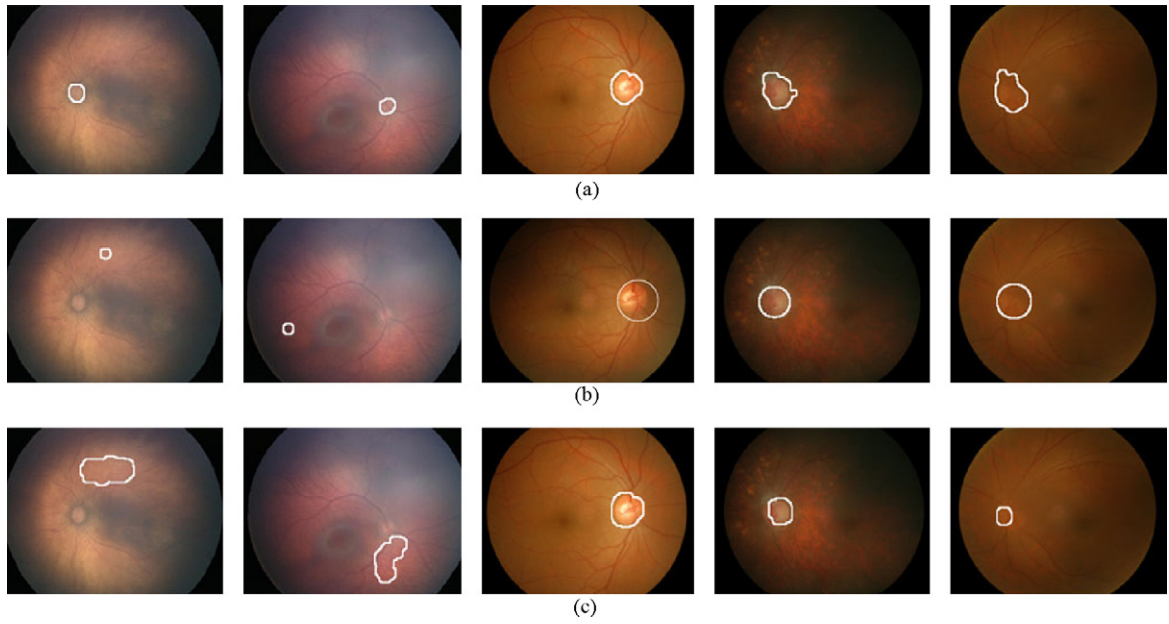
Fig. 11. Detection results at 40% of the original size. Row (a) the proposed method, (b) Circular Hough Transform and (c) morphological operations.
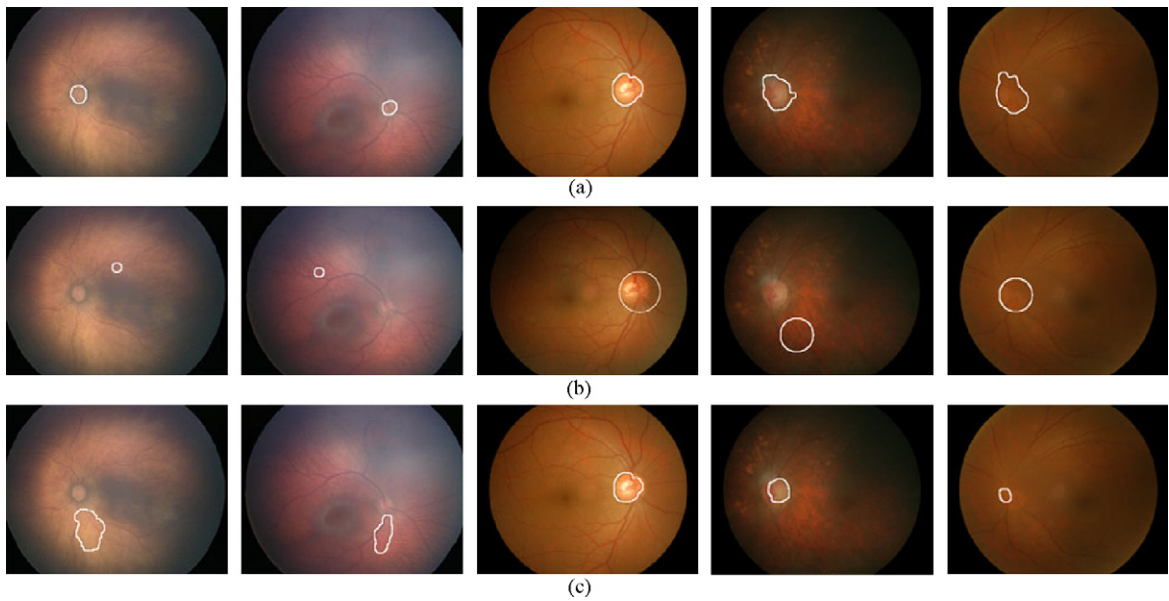

Fig. 12. Detection results, 80% of the original size. (a) the proposed method, (b) Circular Hough Transform and (c) morphological operations.

Table 5
OD detection on cropped images.

Method	Average sensitivity (%)	Average PPV (%)
The proposed method	85.37	82.87
Morphological operator	37.16	78.56
Circular Hough Transform	50.08	40.59

Table 6
Detection results of adults' noisy retinal images (105 images with clear OD boundary).

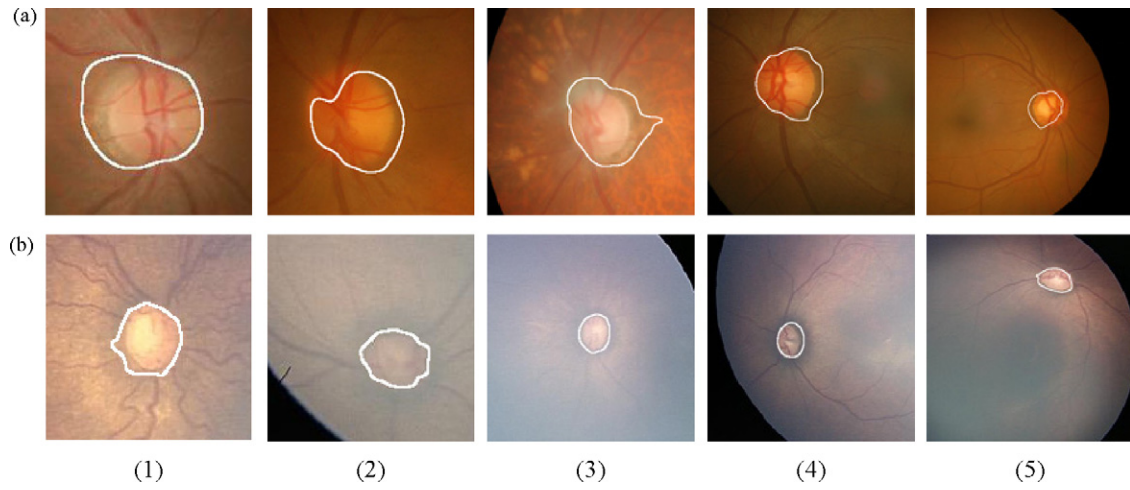| Noise	Proposed method		Morphological operator		Circular Hough Transform	
	Sensitivity	PPV	Sensitivity	PPV	Sensitivity	PPV
1%	78.74	65.02	90.48	59.59	78.41	87.00
5%	72.58	64.74	67.55	49.86	76.80	85.11
10%	70.47	60.69	4.68	4.49	77.72	83.64

Fig. 13. OD detection results of cropped images (note that images displayed here are resized for presentation purposes). (a) Sizes of the images from (1) to (5) are 170×170, 250×250, 340×340, 420×420 and 660×660 pixels, respectively. (b) Sizes of the images from (1) to (5) are 140×140, 160×160, 300×300, 360×360 and 450×450 pixels, respectively.
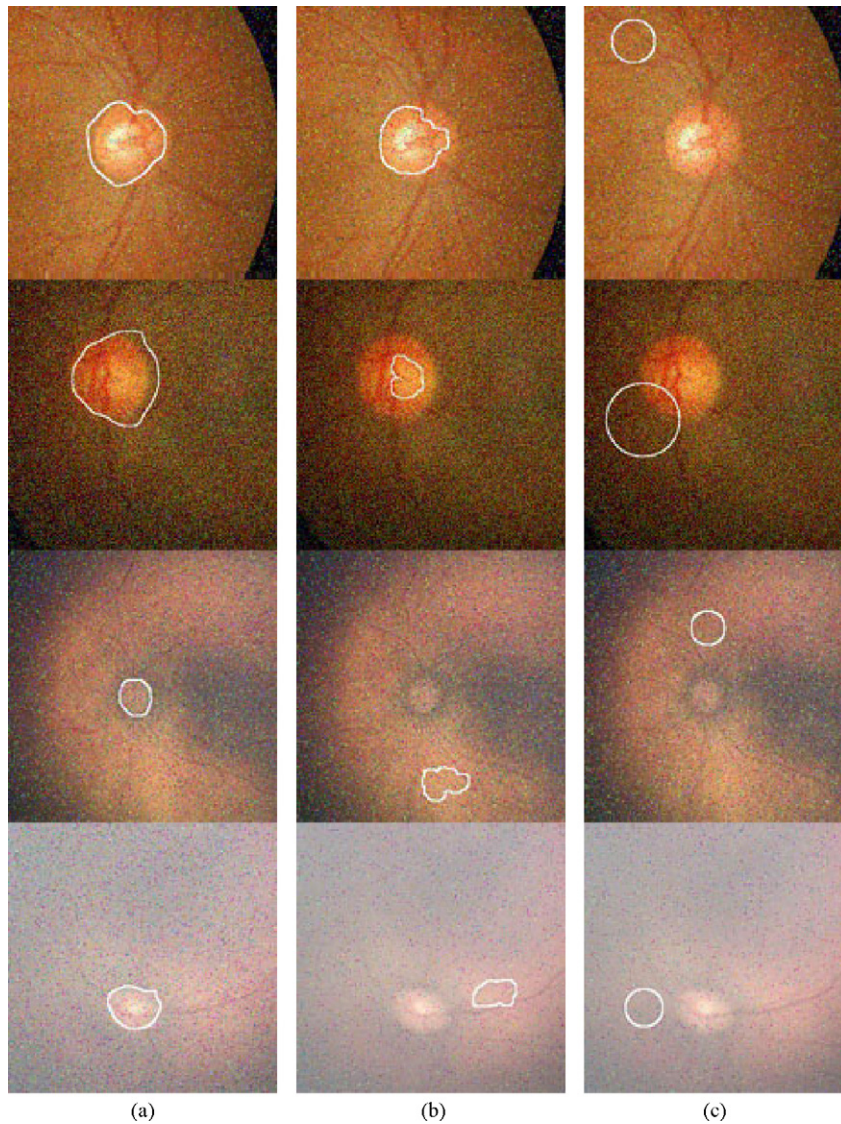

Fig. 14. OD detection for retinal images corrupted by 10% salt-and-pepper noise. Images in rows 1 and 2 are from A1. Row 3 is from B1 and Row 4 is from B2. (a)–(c) Detection results of our proposed method, Morphological operations and Circular Hough transform respectively.

Table 7
Detection results of adults' noisy retinal images (18 images with faint OD boundary).

Noise	Proposed method		Morphological operator		Circular Hough Transform	
	Sensitivity	PPV	Sensitivity	PPV	Sensitivity	PPV
1%	52.37	56.16	79.86	31.26	33.16	31.86
5%	52.08	56.11	32.81	18.13	36.62	35.51
10%	50.11	52.13	3.35	4.84	29.92	23.92

Table 8
Detection results of ROP noisy retinal images (60 images with clear OD boundary).

Noise	Proposed method		Morphological operator		Circular Hough Transform	
	Sensitivity	PPV	Sensitivity	PPV	Sensitivity	PPV
1%	65.78	83.68	17.86	13.32	2.74	5.49
5%	60.45	83.42	8.68	8.53	5.62	6.95
10%	54.53	72.34	1.39	2.03	7.18	10.82

Table 9
Detection results of ROP noisy retinal images (31 images with faint OD boundary).

Noise	Proposed method		Morphological operator		Circular Hough Transform	
	Sensitivity	PPV	Sensitivity	PPV	Sensitivity	PPV
1%	55.34	38.42	10.55	9.53	6.01	6.66
5%	54.89	38.55	5.95	8.57	0.72	3.23
10%	52.18	37.04	0.78	0.65	0.27	0.35

ing the scale-space tree construction, the noise is reduced. To make a fair comparison we preprocess the images using a 3x3 median filter before the morphological operator and the Circular Hough Transform are applied.

3.4. Experiment 4: outliers

Finally, the algorithm was tested on outliers shown in Figs. 15 and 16. The image in Fig. 15 is characterized by a different colour spectrum and dominant white lesions. Even though our first predicted result is incorrect (Fig. 15a), the second blob predicts the OD correctly (Fig. 15b). The algorithm fails because the compactness and brightness of the first candidate blob are much higher than those of the actual OD. Besides, the entropy of the false blob is similar to the real entropy of the actual OD with dominant blood vessels in the middle of the blob.

Fig. 16 shows the case when all the algorithms including the proposed one fail. The optic disc can barely be seen, appearing volcano-like and darker than its perimeter. The boundary of the OD is faint and the intensity of the area close to the OD is not uniform. We believe that even these cases can be treated by our algorithm if it were combined with a vessel-tracing procedure. However, the outliers remain an open problem.

In our experiment, all algorithms are implemented using MATLAB on Windows XP SP3. The average runtime on an Intel Core 2 Duo P8400 2.4 GHz CPU with ram DDR2 2GB is shown in Table 10.
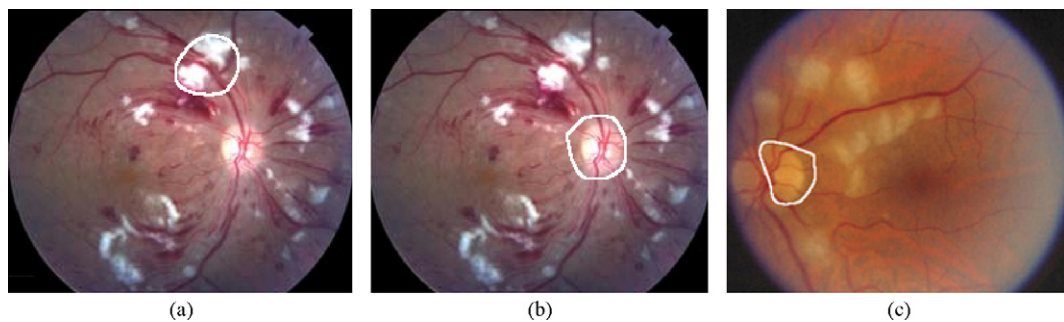

Fig. 15. The OD detection results of retinal images with white lesions and different colour base from normal test sets.
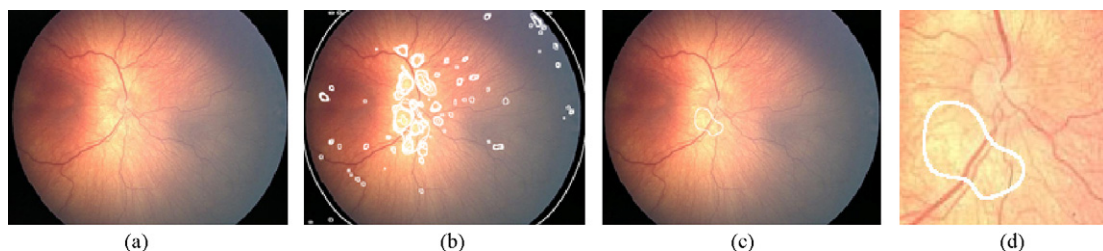

Fig. 16. Example of fault detection. (a) Original image (b) all extracted blobs overlaid on the original image (c) the most significant blob based on proposed method and (d) the close-up in OD area.

Table 10
Performance of the proposed algorithm.

Sets of images	Average time (s)		
	The proposed method	Morphological operator	Circular Hough Transform
Adult retinal images	161.79	1.24	13.21
ROP images	138.24	1.05	10.92
Cropped images	75.44	0.78	8.21
Adult retinal images with noise	223.15	1.25	13.23
ROP with noise	215.72	1.06	10.93

4. Conclusions and discussion

A simple and efficient, parameter free method to detect the optic disc is proposed. The OD candidates are selected from significant scale-space blobs. Three descriptors, namely, compactness, entropy and blob brightness are extracted from each blob. The OD is then identified by three different classifiers, namely decision tree, regression based classifier and majority voting. The results obtained by the three classifiers indicate a low sensitivity to the classification threshold. The algorithm has been verified with 214 infant and adult retinal images supplemented with experts' hand-drawn ground truths. The accuracy of the proposed algorithm is comparable with the accuracy of the standard OD detection methods when the standard procedures are trained. However, the method outperforms the conventional schemes when fed with images obtained in different conditions. These conclusions are supported by an additional series of experiments on resized, cropped and noisy images. The high detection rate and the parameter-free nature of the algorithm make it possible to suggest a hardware implementation for an online OD detection.

Acknowledgements

References

[1] Hubbard LD, Brothers RJ, King WN, Clegg LX, Klein R, Cooper LS, et al. Methods for evaluation of retinal microvascular abnormalities associated with hypertension/sclerosis in the atherosclerosis risk in communities study. Ophthalmology 1999;106:2269–80.

[2] Foracchia M, Grisan E, Ruggeri A. Detection of optic disc in retinal images by means of a geometrical model of vessel structure. IEEE Trans Med Imaging 2004;23:1189–95.

[3] Akita K, Kuga H. A computer method of understanding ocular fundus images. Pattern Recognit 1982;15:431–43.

[4] Lalonde M, Beaulieu M, Gagnon L. Fast and robust optic disc detection using pyramidal decomposition and Hausdorff-based template matching. IEEE Trans Med Imaging 2001;20:1193–200.

[5] Jelinek HF, Depardieu C, Lucas C, Cornforth D, Huang W, Cree MJ. Towards vessel characterisation in the vicinity of the optic disc in digital retinal images. In: Proceedings of the image and vision computing conference. 2005.

[6] Kong HJ, Kim SK, Seo JM, Park KH, Chung H, Park KS, et al. Three dimensional reconstruction of conventional stereo optic disc image. In: Annual international conference of the IEEE EMBS. 2004. p. 1229–32.

[7] Cox MJ, Wood ICJ. Computer-assisted optic nerve head assessment. Ophthal Physiol Opt 1991;11:27–35.

[8] Moris DT, Cox MJ, Wood ICJ. Automated extraction of the optic nerve head rim. In: American association of optometrists annual conference. 1993.

[9] Lee S. Visual monitoring of glaucoma, Ph.D., Robotics Research Group Department of Engineering Science, University of Oxford; 1991.

[10] Osareh A, Mirmehdi M, Thomas B, Markham R. Colour morphology and snakes for optic disc localisation. In: The 6th medical image understanding and analysis conference. 2002. p. 21–4.

[11] Mendels F, Heneghan C, Thiran JP. Identification of the optic disc boundary in retinal images using active contours. In: Proc IMVIP Conf. 1999. p. 103–15.

[12] Chanwimaluang T, Fan G. An efficient algorithm for extraction of anatomical structures in retinal images. In: IEEE international conference on image processing. 2003. p. 1093–6.

[13] Sinthanayothin C, Boyce JF, Cook HL, Williamson TH. Automated localization of the optic disc, fovea, and retinal blood vessels from digital color fundus images. Br J Ophthalmol 1999;83:902–10.

[14] Li H, Chutatape O. Automatic location of optic disc in retinal images. IEEE ICIP 2001:837–40.

[15] Li H, Chutatape O. Boundary detection of optic disc by a modified ASM method. Pattern Recognit 2003;36:2093–104.

[16] Corona E, Mitra S, Wilson M, Krile T, Kwon YH, Soliz P. Digital stereo image analyzer for generating automated 3-D measures of optic disc deformation in glaucoma. IEEE Trans Med Imaging 2002;21:1244–53.

[17] Niemeijer M, Abramoff MD, Van GB. Segmentation of the optic disc, macula and vascular arch in fundus photographs. IEEE Trans Med Imaging 2007;26:116–27.

[18] Tobin KW, Chaum E, Govindasamy VP, Karnowski TP, Sezer O. Characterization of the optic disc in retinal imagery using a probabilistic approach. Proc SPIE 2006.

[19] Kavitha D, Shenbaga DS. Automatic detection of optic disc and exudates in retinal images. In: IEEE Int. conf. on intelligent sensing and information processing (ICISIP). 2005. p. 501–6.

[20] Sopharak A, Uyyanonvara B, Barman S, Williamson TH. Automatic detection of diabetic retinopathy exudates from non-dilated retinal images using mathematical morphology methods. Comput Med Imaging Graph 2008:720–7.

[21] Sekhar S, Al-Nuaimy W, Nandi AK. Automated localisation of retinal optic disc using Hough transform. In: The 5th IEEE international symposium on biomedical imaging: from nano to macro. 2008. p. 1577–80.

[22] Xiaolu Z, Rangaraj MR. Detection of the optic disc in images of the retina using the Hough transform. In: The 30th annual international conference of the ieee engineering in medicine and biology society. 2008. p. 3546–9.

[23] Thongnuch V, Uyyanonvara B. Automatic optic disc detection from low contrast retinal images of ROP infant using GVF snake. Suranaree J Sci Technol 2007:223–6.

[24] Chrástek R, Skokan M, Kubec̆ka L, Wolf M, Donath K, Jan J, et al. Multimodal retinal image registration for optic disk segmentation. Methods Inf Med 2004;43:336–42.

[25] Niemeijer M, Abràmoff MD, Ginneken B. Fast detection of the optic disc and fovea in color fundus photographs. J Med Image Anal 2009;13(6):859–70.

[26] Winder RJ, Morrow PJ, McRitchie IN, Bailie JR, Hart PM. Algorithms for digital image processing in diabetic retinopathy. Comput Med Imaging Graph 2009;33(8):608–22.

[27] Kondo H, Kouda T. Detection of pneumoconiosis rounded opacities using neural network. In: Joint 9th IFSA world congress and 20th NAFIPS international conference 3. 2001. p. 1581–5.

[28] Wang S, Wang M. A new detection algorithm (NDA) based on fuzzy cellular neural networks for white blood cell detection. IEEE Trans Inform Technol Biomed 2006;10:5–10.

[29] Witkin AP. Scale-space filtering. In: In proc. 8th int. joint conf. art. intell. 1983. p. 1019–22.

[30] Koenderink JJ, Doorn AJv. Generic neighbourhood operators. IEEE Trans Pattern Anal Mach Intell 1992:597–605.

[31] Lindeberg T. Detecting salient blob-like image structures and their scales with a scale-space primal sketch: a method for focus-of-attention. Int J Comput Vision 1993:283–318.

[32] Lindeberg T. Scale-space theory in computer vision the kluwer international series in engineering and computer science. Dordrecht, Netherlands: Kluwer Academic Publishers; 1994.

[33] Hoover A, Goldbaum M. Locating the optic nerve in a retinal image using the fuzzy convergence of the blood vessels. IEEE Trans Med Imaging 2003;22(8):951–8.

[34] Trucco E, Kamat PJ. Locating the optic disc in retinal images via plausible detection and constraint satisfaction. In: Proceedings of the international ieee conference on image processing (ICIP'04). 2004. p. 155–8.

[35] Novo J, Penedo MG, Santos J. Localisation of the optic disc by means of GA-optimised topological active nets. Image Vision Comput 2009;27:1572–84.

[36] Chaudhuri S, Chatterjee S, Katz N, Nelson M, Goldbaum M. Detection of blood vessels in retinal images using two-dimensional matched filters. IEEE Trans Med Imaging 1989;8:263–9.

[37] Sánchez CI, García M, Mayo A, López MI, Hornero R. Retinal image analysis based on mixture models to detect hard exudates. Med Image Anal 2009;13(4):650–8.

[38] Welfer D, Scharcanski J, Kitamura CM, Pizzol MMD, Ludwig LWB, Marinho DR. Segmentation of the optic disc in color eye fundus images using an adaptive morphological approach. Comput Biol Med 2010;40(2):124–37.

[39] Perez-Rovira A, Trucco E. Robust optic disc location via combination of weak detectors. In: Proceedings of the 30th annual international conference of the IEEE engineering in medicine and biology society. 2008. p. 3542–5.

[40] Lowell J, Hunter A, Steel D, Basu A, Ryder R, Fletcher E. Optic nerve head segmentation. IEEE Trans Med Imaging 2004:256–64.

[41] Quinlan JR. C4. 5: programs for machine learning. Morgan Kaufmann Publishers; 1993.
[42] Gonzales RC, Woods RE. Digital image processing. second ed. NJ: Addison-Wesley publishing Co.; 2002. pp. 65–107.

Cattleya Duanggate received her B.Eng. and M.Eng. degrees in Computer Engineering from Chiang Mai University and King Mongkut's Institute of Technology Ladkrabang, Thailand, in 2000 and 2003, respectively. She is currently a doctor degree student at Sirindhorn International Institute of Technology, Thammasat University. Her research interests include medical image processing and computer vision.

Bunyarit Uyyanonvara is currently an associate professor in Information Technology at Sirindhorn International Institute of Technology, Thammasat University. He received his B.Sc. (1st Class Honors) in Science from Prince of Songkhla University, in 1995 and his Ph.D. in Medical Image Processing from King's College, University of London, in 2000.

Stanislav S. Makhanov is currently an associate professor in Information Technology at Sirindhorn International Institute of Technology, Thammasat University. He received his M.Sc degree in Applied Mathematics from the Moscow State University in 1981 and Dr.Sc. degree in Applied Mathematics from the Computer Center of the Russian Academy of Science in 1988. From 1981 to 1994, he worked at the Computer Center of the Russian Academy of Science as Research Fellow, assistant professor and associate professor. From 1994 to 1999 he worked at the King Mongkut's Institute of Technology, Ladkrabang, Thailand as visiting professor and at the Asian Institute of Technology as associated faculty member. His present research interest includes new numerical methods for Computational Fluid Dynamics, Robotics and Image Processing.

Sarah Barman qualifications include a B.Sc. in physics from Essex University, an M.Sc. in applied optics from Imperial College, University of London and a Ph.D. in optical physics from King's College, University of London. Since 2000, Dr. Barman has been based at the Digital Imaging Research Centre at Kingston University and is currently investigating medical imaging algorithms, based on her experience of image processing and optical modeling techniques for use on a range of ophthalmic images.

Thomas H. Williamson Consultant Ophthalmologist and Vitreoretinal Specialist in London, UK. He is a senior consultant Ophthalmologist at St. Thomas' Hospital, London, Queen Mary's Hospital, Sidcup, Kent, and an Honorary Clinical Lecturer at King's College, London. His specialist area of interest is retinal disease and surgery. He also has an over 20 years experience in the care of the eye and 13 years as a vitreoretinal specialist.